

## Article

# Four-Objective Optimization of an Irreversible Stirling Heat Engine with Linear Phenomenological Heat-Transfer Law

Haoran Xu <sup>1,2,3</sup> , Lingen Chen <sup>1,2,3,\*</sup> , Yanlin Ge <sup>1,2,3</sup> and Huijun Feng <sup>1,2,3</sup><sup>1</sup> Institute of Thermal Science and Power Engineering, Wuhan Institute of Technology, Wuhan 430205, China<sup>2</sup> Hubei Provincial Engineering Technology Research Center of Green Chemical Equipment, Wuhan 430205, China<sup>3</sup> School of Mechanical & Electrical Engineering, Wuhan Institute of Technology, Wuhan 430205, China\* Correspondence: [lingenchen@hotmail.com](mailto:lingenchen@hotmail.com)

**Abstract:** This paper combines the mechanical efficiency theory and finite time thermodynamic theory to perform optimization on an irreversible Stirling heat-engine cycle, in which heat transfer between working fluid and heat reservoir obeys linear phenomenological heat-transfer law. There are mechanical losses, as well as heat leakage, thermal resistance, and regeneration loss. We treated temperature ratio  $x$  of working fluid and volume compression ratio  $\lambda$  as optimization variables, and used the NSGA-II algorithm to carry out multi-objective optimization on four optimization objectives, namely, dimensionless shaft power output  $\bar{P}_s$ , braking thermal efficiency  $\eta_s$ , dimensionless efficient power  $\bar{E}_p$  and dimensionless power density  $\bar{P}_d$ . The optimal solutions of four-, three-, two-, and single-objective optimizations are reached by selecting the minimum deviation indexes  $D$  with the three decision-making strategies, namely, TOPSIS, LINMAP, and Shannon Entropy. The optimization results show that the  $D$  reached by TOPSIS and LINMAP strategies are both 0.1683 and better than the Shannon Entropy strategy for four-objective optimization, while the  $D$ s reached for single-objective optimizations at maximum  $\bar{P}_s$ ,  $\eta_s$ ,  $\bar{E}_p$ , and  $\bar{P}_d$  conditions are 0.1978, 0.8624, 0.3319, and 0.3032, which are all bigger than 0.1683. This indicates that multi-objective optimization results are better when choosing appropriate decision-making strategies.

**Keywords:** irreversible Stirling heat engine; finite time thermodynamics; mechanical efficiency theory; linear phenomenological heat-transfer law; mechanical losses; multi-objective optimization



**Citation:** Xu, H.; Chen, L.; Ge, Y.; Feng, H. Four-Objective

Optimization of an Irreversible Stirling Heat Engine with Linear Phenomenological Heat-Transfer Law. *Entropy* **2022**, *24*, 1491.

<https://doi.org/10.3390/e24101491>

Academic Editor: Michel Feidt

Received: 15 September 2022

Accepted: 17 October 2022

Published: 19 October 2022

**Publisher's Note:** MDPI stays neutral with regard to jurisdictional claims in published maps and institutional affiliations.



**Copyright:** © 2022 by the authors. Licensee MDPI, Basel, Switzerland. This article is an open access article distributed under the terms and conditions of the Creative Commons Attribution (CC BY) license (<https://creativecommons.org/licenses/by/4.0/>).

## 1. Introduction

Finite time thermodynamics (FTT) [1–30] has developed and emerged since the mid-1970s. With the continuous development and improvement of the theory, its research objects have expanded from Carnot heat engine to almost all engineering thermal devices and systems, which include the Stirling heat engine (SHE). Blank et al. [31] considered the finiteness of temperature difference between working fluid (WF) and heat reservoir to establish a FTT model of an endoreversible SHE cycle and optimized its power output ( $P$ ). Chen et al. [32,33] studied SHE with imperfect regeneration, analyzed the influence of regeneration loss, and reached thermal efficiency ( $\eta$ ) at maximum  $P$  [32], then obtained the  $\eta$  bound of the solar-driven SHE cycle [33]. Wu et al. [34] studied SHE cycle with heat-transfer (HT) loss and regeneration loss, and derived the expressions of cycle  $P$  and  $\eta$ . Tlili et al. [35,36] studied the influences of relevant parameters on  $\eta$  of a SHE cycle at maximum  $P$ , and found that increasing specific heat capacity of heat sink would cause the SHE cycle to have higher  $P$ . Li et al. [37] performed optimization on  $P$  of a solar-powered SHE cycle and reached the  $\eta$  at maximum  $P$ . Ahmadi et al. [38] studied the influences of heat-exchanger and regenerator parameters on  $P$  and  $\eta$  of a SHE cycle. Ahmed et al. [39] studied the influences of HT and flow frictions of a regenerator, a heater, and a cooler on  $P$  and  $\eta$  of a beta-type SHE cycle. Ramachandran et al. [40] studied the influences of different types of

WF and regenerator materials on cycle  $P$  and  $\eta$  of a solar low-temperature differential SHE cycle with regeneration loss. Ahadi et al. [41] studied the influences of coating type and thickness on  $P$  and  $\eta$  of a SHE cycle, and pointed out that for different types of coating,  $\eta$  was enhanced with increased coating thickness. De Moura et al. [42] studied the influences of regenerator efficiency, compression ratio, HT coefficient, engine frequency, piston stroke, and area on performance of a space power SHE cycle, and optimized the  $P$  and  $\eta$ . Purkait and Biswas [43] studied the effect on  $P$  and  $\eta$  of a quantum SHE cycle. Kitaya and Isoke [44] optimized the effect on  $P$  and  $\eta$  of a nano-scale  $\beta$ -type SHE cycle.

Power density (PD) was first proposed by Sahin et al. [45], and they used it to perform optimization of a Joule-Brayton cycle. The research showed that compared with the maximum  $P$  conditions, the heat engine had smaller dimensions and higher  $\eta$  at maximum PD optimization. Chen et al. [46] studied an endoreversible closed Brayton cycle with thermal resistance, and derived the expression of PD. Ust [47] compared the  $\eta$  of an Atkinson heat-engine cycle with temperature ratio and internal irreversibility loss at maximum  $P$  and maximum PD. Gonca [48] studied the influences of internal irreversibility loss and HT loss on a dual-Atkinson cycle, and derived its maximum dimensionless  $P$ ,  $\eta$ , and dimensionless PD. Karakurt et al. [49] performed optimization on the PD characteristics of a supercritical CO<sub>2</sub> Brayton cycle.

When studying and optimizing the performance of heat engines, one can neither pursue  $\eta$  and ignore  $P$ , nor consider  $P$  without considering  $\eta$ . Therefore, in addition to the basic output rate, Yan [50] used a product of cycle  $P$  and  $\eta$  ( $P\eta$ ) as an optimization objective to perform optimization on an endoreversible Carnot heat-engine cycle. Yilmaz [51] named it efficient power (EP) and pointed out that a heat engine designed at the maximum EP conditions may have better  $P$  than maximum PD optimization. Besides, the maximum EP optimization had a significant  $\eta$  advantage with respect to maximum  $P$  optimization. Later, more and more scholars applied it to various heat-engine cycles on the basis of EP optimization objective (OO) [52–55].

With the increase in OOs, conflicts will occur among various OOs; single-objective optimization will improve one OO but worsen another. In order to take more OOs into account and reach the optimal design scheme, one must perform multi-objective optimization (MOO) research on different thermodynamic cycles. For SHE cycles, Ahmadi et al. [56–58] had conducted extensive MOO research on different SHE cycles. Luo et al. [59] took power loss,  $P$ , and  $\eta$  as OOs to perform MOO research on SHE cycles, and the results showed that MOO not only improved the  $P$  and  $\eta$ , but also significantly reduced the power loss caused by flow resistance. Punnathanam and Kotecha [60] took entropy generation rate,  $P$ , and  $\eta$  as OOs to perform MOO research on SHE cycles. Hooshang et al. [61] applied third-order thermodynamic analysis to optimize the performance of SHE cycles, performed MOO research on the cycle with two OOs of  $P$  and regenerator differential pressure, and compared the results reached by three decision-making strategies. Dai et al. [62] performed MOO research on a regenerative SHE cycle with three OOs of ecological coefficient of performance,  $P$ , and  $\eta$ . Ye et al. [63] took  $P$ ,  $\eta$ , and exergy efficiency as OOs to perform MOO research on SHE cycles. Shah et al. [64] considered volume ratio, temperature ratio, and surface area ratio of nanoscale SHE cycles, and performed MOO research on the cycles' ecological coefficient of performance,  $\eta$  and entropy generation rate. Shakouri et al. [65] performed MOO research on solid oxide fuel cell-SHE cycles with three OOs of  $P$ , exergy efficiency, and exergy destruction density. Ahmed et al. [66] considered such parameters as heat-source temperature, engine frequency, average effective pressure, piston diameter, and regenerator grid line diameter, and took  $P$ ,  $\eta$ , and losses as OOs to perform MOO on SHE cycles.

Senft [67,68] proposed mechanical efficiency theory, offering the upper limit of the mechanical efficiency of heat engines, and pointed out that the ideal SHE has maximum mechanical efficiency in the reciprocating heat engine; then, he combined it with FTT to establish a new SHE cycle model which was different from the conventional FTT model. He derived expressions of shaft power output ( $P_s$ ) and braking thermal efficiency ( $\eta_s$ ), and

analyzed the effect of mechanical losses and HT loss with Newtonian heat-transfer law (HTL) ( $q \propto \Delta T$ ). On the basis of the model established by Senft [67,68], Xu et al. [69] proposed dimensionless shaft power output ( $\bar{P}_s$ ),  $\eta_s$ , dimensionless EP ( $\bar{E}_p$ ), and dimensionless ecological function, then took them as OOs to perform MOO research on SHE cycles.

Actually, the heat transfer between WF and heat reservoir does not completely obey Newton's HTL. When options governed by the HTL change, the performance of the heat engine will also change. Therefore, in addition to Newton's HTL, some scholars have studied the influences of linear phenomenological, radiation, and generalized radiation HTLs on  $P$  and  $\eta$  of the endoreversible heat engine [70–72]. The authors of references [73,74] studied  $P$  and  $\eta$  of an endoreversible Carnot heat engine with generalized convection HTL. Chen et al. [75] studied the maximum  $P$  and maximum  $\eta$  of an irreversible Carnot heat engine based on a universal HTL  $q \propto (\Delta T^n)^m$ . Li and Chen [76] and Chen and Xia [77] found the optimal configuration of heat engines with  $q \propto (\Delta T^n)^m$  [76] and more universal HTL [77]. Ding et al. [78] optimized the  $P_s$  and  $\eta_s$  characteristics of irreversible SHE cycles with linear phenomenological HTL.

On the basis of references [67,68], this study will analyze the effects of mechanical losses, as well as heat leakage, regeneration loss, and thermal resistance on SHE cycles with linear phenomenological HTL ( $q \propto \Delta(T^{-1})$ ). The temperature ratio ( $x$ ) of the WF and volume compression ratio ( $\lambda$ ) of the cycle will be selected as optimization variables, then the NSGA-II algorithm [79–82] will be applied to perform MOO on four OOs, that is,  $\bar{P}_s$ ,  $\eta_s$ ,  $\bar{E}_p$ , and dimensionless PD ( $\bar{P}_d$ ). The Pareto optimal solution of four-, three-, two-, and single-objective optimizations will be reached, and the optimal scheme will be reached by selecting the minimum deviation indexes ( $D$ ) [83] with TOPSIS [84–86], LINMAP [87,88], and Shannon Entropy [89,90] decision-making strategies.

Compared with the previous MOO research of different SHE cycles [56–66,69], the major contribution of this paper is that, firstly, the effects of the linear phenomenological HTL, which is different from Newton's HTL, on the performance of the SHE are studied, and the expressions of four OOs are derived. It is also found that  $P_s$ ,  $\eta_s$ , and  $E_p$  are obviously different from those in reference [69] referring to Newton's HTL; secondly, a more realistic cycle model with various heat and mechanical losses is adopted; and, finally, different OOs are introduced. In addition to  $\bar{P}_s$ ,  $\eta_s$ , and  $\bar{E}_p$ , this paper takes  $\bar{P}_d$  as the fourth OO, so the optimization results will be significantly different from the previous research.

## 2. Model of SHE Cycle and OOs

An irreversible SHE cycle model [67] is presented in Figure 1.  $T_H$  and  $T_L$  are temperatures of heat source and heat sink, WF of the cycle is an ideal gas,  $R$  is a regenerator,  $Q_i$  is heat leakage,  $T_1$  is temperature of WF in the expansion process, and  $T_2$  is the temperature of WF in the compression process.

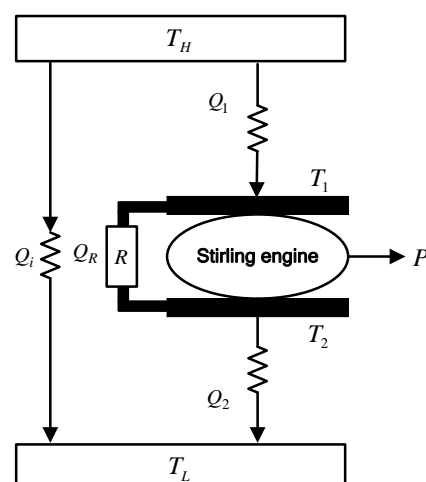


Figure 1. Irreversible SHE cycle model.

On the basis of thermodynamic properties of ideal gas and linear phenomenological HTL ( $q \propto \Delta(T^{-1})$ ), the heats transferred between the heat reservoir and the WF can be expressed as follows:

$$Q_1 = \alpha \left( \frac{1}{T_1} - \frac{1}{T_H} \right) t_1 = nR_u T_1 \ln \lambda \quad (1)$$

$$Q_2 = \beta \left( \frac{1}{T_L} - \frac{1}{T_2} \right) t_2 = nR_u T_2 \ln \lambda \quad (2)$$

where  $\alpha$  and  $\beta$  are HT coefficients,  $t_1$  and  $t_2$  are time duration of the expansion and compression process,  $n$  is mole number of the WF,  $\lambda = v_2/v_1$  is volume compression ratio (equal to the maximum specific volume ratio of the cycle), and  $R_u$  is the universal gas constant of WF.

The regeneration loss ( $\Delta Q_R$ ) of the cycle can be expressed as:

$$\Delta Q_R = nC_v(1 - \eta_R)(T_1 - T_2) \quad (3)$$

where  $\eta_R$  is the efficiency of the regenerator and  $C_v$  is the constant volume specific heat capacity of WF.

Sorting out Equations (1) and (2),  $t_1$  and  $t_2$  can be expressed as:

$$t_1 = \frac{nR_u T_1 \ln \lambda}{\alpha \left( \frac{1}{T_1} - \frac{1}{T_H} \right)}, \quad t_2 = \frac{nR_u T_2 \ln \lambda}{\beta \left( \frac{1}{T_L} - \frac{1}{T_2} \right)} \quad (4)$$

The WF temperature ( $T$ ) varies uniformly with time ( $t$ ) during the regeneration process, and satisfies the following equation:

$$\frac{dT}{dt} = \pm K_1 \quad (5)$$

where “+” indicates the heating process and “−” indicates the cooling process;  $K_1$  ( $K_1 > 0$ ) is only determined by the material of the regenerator.

By integrating Equation (5), the time durations of the regenerative process ( $t_3$  and  $t_4$ ) can be expressed as:

$$t_3 = \frac{(T_1 - T_2)}{K_1} = t_4 \quad (6)$$

According to Equations (4) and (6), the cycle period  $\tau$  can be expressed as:

$$\tau = \frac{nR_u T_1 \ln \lambda}{\alpha(T_1^{-1} - T_H^{-1})} + \frac{nR_u T_2 \ln \lambda}{\beta(T_L^{-1} - T_2^{-1})} + \frac{2(T_1 - T_2)}{K_1} \quad (7)$$

The heat leakage can be expressed as:

$$Q_i = C_i \left( \frac{1}{T_L} - \frac{1}{T_H} \right) \tau \quad (8)$$

where  $C_i$  is the heat-leakage coefficient.

According to Equations (1)–(3) and (8), the heat ( $Q_H$ ) supplied by the heat source and heat ( $Q_L$ ) released to the heat sink can be expressed as, respectively:

$$Q_H = Q_1 + Q_i + \Delta Q_R \quad (9)$$

$$Q_L = Q_2 + Q_i + \Delta Q_R \quad (10)$$

The  $P$  and  $\eta$  can be expressed as:

$$P = \frac{Q_H - Q_L}{\tau} = \frac{(Q_1 - Q_2)}{\tau} \quad (11)$$

$$\eta = \frac{Q_H - Q_L}{Q_H} = \frac{Q_1 - Q_2}{Q_1 + Q_i + \Delta Q_R} \tag{12}$$

According to the expressions of  $Q_H$ ,  $Q_L$ ,  $\Delta Q_R$ ,  $Q_i$ , and  $\tau$ , the  $P$  and  $\eta$  can be further expressed as:

$$P = \frac{n\alpha R_u \ln \lambda K_1 (1-x)(T_2 - T_L)(xT_H - T_2)}{2\alpha(1-x)(T_2 - T_L)(xT_H - T_2) + nR \ln \lambda K_1 T_2 [T_2(T_H - \delta^2 x T_L) + T_H T_L(\delta^2 x^2 - 1)]} \tag{13}$$

$$\eta = \frac{n\alpha R_u \ln \lambda K_1 T_H T_L (1-x)(T_2 - T_L)(xT_H - T_2)}{\{2\alpha C_i (T_H - T_L)(x-1)(T_2 - T_L)(xT_H - T_2) - nR_u \ln \lambda K_1 T_2 C_i (T_H - T_L)[T_2(T_H - \delta^2 x T_L) + T_H T_L(\delta^2 x^2 - 1)] + n\alpha K_1 T_H T_L (T_2 - T_L)(T_2 - xT_H)[R_u \ln \lambda + C_v(x-1)(\eta_R - 1)]\}} \tag{14}$$

where  $\delta = \sqrt{\alpha/\beta}$ , and  $x = T_2/T_1$  is the WF temperature ratio during the isothermal process.

According to references [30–34], the PD can be expressed as:

$$P_d' = \frac{P}{v_{\max}} = \frac{P}{v_2} = \frac{P}{\lambda v_1} \tag{15}$$

The optimal temperature for optimal  $P$ ,  $\eta$ , and  $P_d'$  can be expressed as follows:

$$T_{2,opt} = \frac{T_H T_L [T_H(1 + \delta x) - T_L \delta(1 + \delta)]}{T_H^2 - \delta T_L^2} \tag{16}$$

Taking the expression of  $T_{2,opt}$  into Equations (13)–(15), the optimal performance expressions of  $P$ ,  $\eta$ , and  $P_d'$  can be expressed as:

$$P = \frac{nR_u \ln \lambda K_1 (-T_H^2 \delta^{-1} + 2T_H T_L - \delta T_L^2)(xT_H - T_L)}{\{2[2T_H T_L(xT_H - T_L) - (xT_H^3 \delta^{-1} - \delta T_L^3) - T_H T_L(\delta x T_L - T_H \delta^{-1})] - nR_u \ln \lambda K_1 T_H T_L (T_H^2 \delta^{-1} - 2T_H T_L + \delta T_L^2)(\delta x^2 + 2x + \delta^{-1})\}} \tag{17}$$

$$\eta = \frac{n\alpha R_u \ln \lambda K_1 T_H T_L (1-x)(xT_H - T_L)^2 (T_H - \delta T_L)(\delta^{-1} T_H - T_L)}{\{2\alpha C_i (T_H - T_L)(x-1)\{x(\delta^{-1} T_H^2 - \delta T_L^2)^2 + [(\delta^{-1} + x)T_H - (x\delta + 1)T_L]^2 T_H T_L + [(\delta^{-1} + x)T_H - (x\delta + 1)T_L](\delta^{-1} T_H^2 - \delta T_L^2)(T_L + x\alpha^2 \delta^{-2} T_H)\} + nR_u \ln \lambda K_1 T_H T_L C_i (T_H - T_L)[(\delta^{-1} + x)T_H - (x\delta + 1)T_L]\{[(\delta^{-1} + x)T_H - (x\delta + 1)T_L](T_H - x\delta^2 T_L) + (T_H^2 - \delta^2 T_L^2)(\delta^{-1} - \delta x^2)\} - n\alpha K_1 T_H T_L (\delta T_L - T_H)(\delta^{-1} T_H - T_L)(xT_H - T_L)^2 [R_u \ln \lambda + C_v(x-1)(\eta_R - 1)]\}} \tag{18}$$

$$P_d' = \frac{nR_u \ln \lambda K_1 (-T_H^2 \delta^{-1} + 2T_H T_L - \delta T_L^2)(xT_H - T_L)}{v_1 \lambda \{2[2T_H T_L(xT_H - T_L) - (xT_H^3 \delta^{-1} - \delta T_L^3) - T_H T_L(\delta x T_L - T_H \delta^{-1})] - nR_u \ln \lambda K_1 T_H T_L (T_H^2 \delta^{-1} - 2T_H T_L + \delta T_L^2)(\delta x^2 + 2x + \delta^{-1})\}} \tag{19}$$

A reciprocating heat-engine model is presented in Figure 2 [68], and the arrow indicates the direction of the work transfer. The mechanical device, flywheel, and buffer space are represented by  $M$ ,  $F$ , and  $B$ , respectively. The atmosphere often serves as the buffer gas in  $B$ . Buffer gas acts on the piston directly and it absorbs and stores energy and returns it to the WF. The arrow indicates the direction of the work transfer.  $W_e$  and  $W_c$  are cycle expansion work and compression work.  $W_+$  is the work conducted by the piston on  $M$ ,  $W_-$  is the work conducted by  $M$  on the piston.  $W_s$  is the cycle shaft work, which is also the useful output work produced by the engine in each cycle. The quantity of the output work for the cycle is determined by mechanism effectiveness ( $e$ ). The ratio of shaft work to indicated work is referred to as mechanical efficiency ( $\eta_{ms}$ ), and Senft pointed out that it cannot exceed as follows for fixed  $x$ ,  $\lambda$ , and  $e$  [68]:

$$\eta_{ms}(e, x, \lambda) = e - S(x, \lambda) \left(\frac{1}{e} - e\right) \tag{20}$$

where:

$$S(x, \lambda) = \begin{cases} 0 & x\lambda \leq 1 \\ \frac{x \ln x - (1+x)[\ln(1+x) - \ln(1+\lambda)] - \ln \lambda}{(1-x) \ln \lambda} & x\lambda > 1 \end{cases} \quad (21)$$

Combining Equations (17), (18) and (20), the  $P_s$  and  $\eta_s$  expressions for the SHE cycle are, respectively:

$$P_s = P\eta_{ms} \quad (22)$$

$$\eta_s = \eta\eta_{ms} \quad (23)$$

Combining Equations (19)–(23), the EP and PD of the SHE cycle with mechanical losses can be expressed as:

$$E_p = P_s\eta_s \quad (24)$$

$$P_d = P_d'\eta_{ms} \quad (25)$$

Consequently, the  $\bar{P}_s$ ,  $\bar{E}_p$ , and  $\bar{P}_d$  can be expressed as:

$$\bar{P}_s = P_s / (P_s)_{\max} \quad (26)$$

$$\bar{E}_p = E_p / (E_p)_{\max} \quad (27)$$

$$\bar{P}_d = P_d / (P_d)_{\max} \quad (28)$$

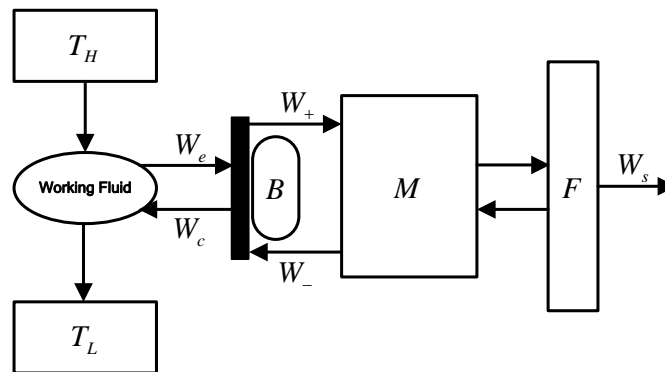


Figure 2. Reciprocating heat-engine model.

### 3. Multi-Objective Optimizations

Problems with two or more OOs are called MOO problems. MOO can improve at least one OO without deteriorating other objectives, and it does not indicate that each OO reaches the maximum. The Pareto optimal solution is the ultimate result of continuous optimization, and the set composed of these solutions is called the Pareto frontier.

The NSGA-II algorithm is used to resolve the MOO problem in this paper, and its flow chart is represented as Figure 3. Taking  $x$  and  $\lambda$  as optimization variables, and  $\bar{P}_s$ ,  $\eta_s$ ,  $\bar{E}_p$ , and  $\bar{P}_d$  are OOs of the cycle, the MOOs are performed on four-, three-, two-, and single-objective by using the NSGA-II algorithm. TOPSIS, LINMAP, and Shannon Entropy decision-making strategies are taken to obtain the optimal scheme by comparing the deviation indexes.

The following parameters are determined by references [67,68]:  $n = 1.0$  mol,  $C_v = 20.77$  J/(mol · K),  $T_H = 800$  K,  $T_L = 300$  K, and  $K_1 = 8.0 \times 10^3$  K/s. The value ranges of the two variables are  $0.375 \leq x \leq 0.775$  and  $1.15 \leq \lambda \leq 7.15$ , respectively.

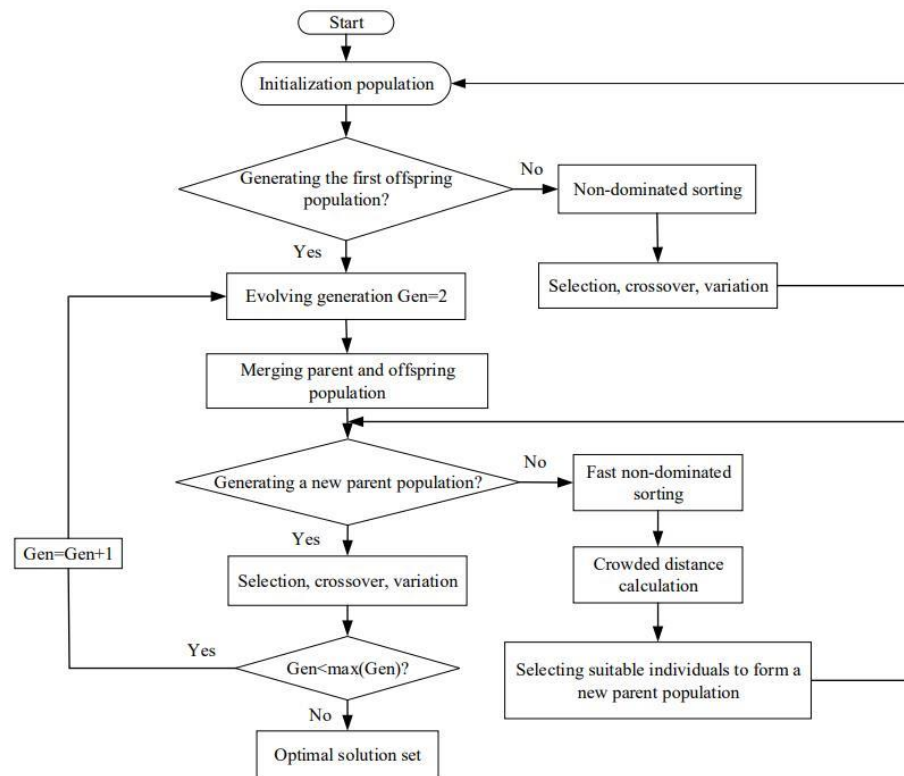


Figure 3. NSGA-II algorithm flow chart.

The NSGA-II algorithm’s configuration parameters are listed in Table 1. The results reached by four-, three-, two-, and single-objective optimizations under three strategies are shown in Table 2. According to Table 2, the values of positive ideal points are 1.000, 1.000, 0.3718, and 1.000, respectively, and the values of negative ideal points are 0.3745, 0.1854, 0.4962, and 0.1442, respectively. At the maximum  $\bar{P}_s$ ,  $\eta_s$ ,  $\bar{E}_p$ , and  $\bar{P}_d$  conditions, the deviation indexes of four single-objective optimizations are 0.1978, 0.8624, 0.3319, and 0.3032, respectively.

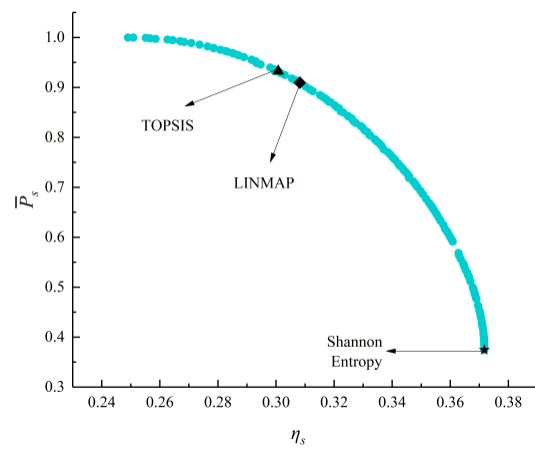
Table 1. NSGA-II algorithm parameters.

| Parameters         | Values |
|--------------------|--------|
| Generations        | 700    |
| Population size    | 300    |
| Pareto fraction    | 0.5    |
| Crossover fraction | 0.8    |

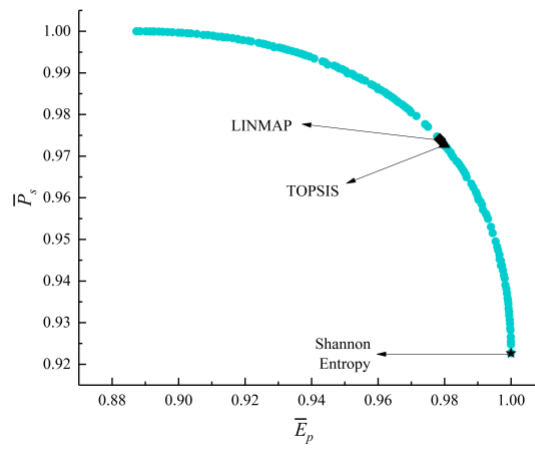
Figure 4 shows the Pareto frontiers reached by corresponding two-objective optimizations ( $\bar{P}_s - \eta_s$ ,  $\bar{P}_s - \bar{E}_p$ ,  $\bar{P}_s - \bar{P}_d$ ,  $\eta_s - \bar{E}_p$ ,  $\eta_s - \bar{P}_d$ , and  $\bar{E}_p - \bar{P}_d$ ). From these six figures, as  $\bar{P}_s$  grows,  $\eta_s$ ,  $\bar{E}_p$ , and  $\bar{P}_d$  will all decline. As  $\eta_s$  grows,  $\bar{E}_p$  and  $\bar{P}_d$  will decline. As  $\bar{E}_p$  grows,  $\bar{P}_d$  will decline. According to Table 2, when MOO is performed on  $\bar{P}_s - \eta_s$ , the deviation index (0.3250) calculated by the TOPSIS strategy is smaller. When MOO is performed on  $\bar{P}_s - \bar{E}_p$ ,  $\bar{P}_s - \bar{P}_d$ ,  $\eta_s - \bar{P}_d$ , and  $\bar{E}_p - \bar{P}_d$ , the deviation indexes (0.2580, 0.2286, 0.1782, and 0.1636) calculated by the LINMAP strategy are smaller. When MOO is performed on  $\eta_s - \bar{E}_p$ , the deviation index (0.3306) calculated by the Shannon Entropy strategy is smaller.

**Table 2.** Results of four-, three-, two-, and single-objective optimizations.

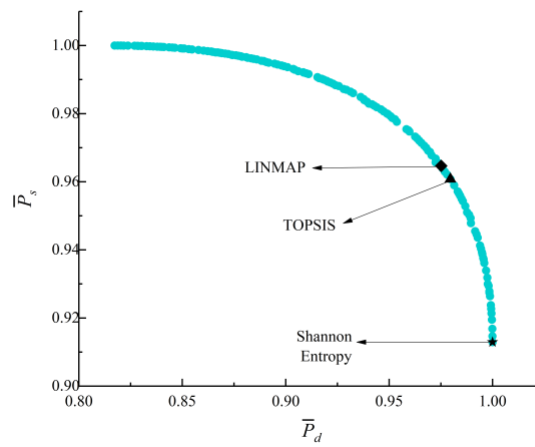
| Optimization Methods   | Decision-Making Strategies | Optimization Variables |           | Optimization Objectives |          |             |             | Deviation Index |
|--|----------------------------|------------------------|-----------|-------------------------|----------|-------------|-------------|-----------------|
|  |                            | $x$                    | $\lambda$ | $\bar{P}_s$             | $\eta_s$ | $\bar{E}_p$ | $\bar{P}_d$ | $D$             |
| Four-objective optimization<br>( $\bar{P}_s, \eta_s, \bar{E}_p,$ and $\bar{P}_d$ ) | LINMAP                     | 0.5815                 | 1.5301    | 0.9608                  | 0.2601   | 0.8905      | 0.8721      | 0.1683          |
|  | TOPSIS                     | 0.5815                 | 1.5301    | 0.9608                  | 0.2601   | 0.8905      | 0.8721      | 0.1683          |
|  | Shannon Entropy            | 0.6610                 | 1.2684    | 0.9128                  | 0.1877   | 0.6103      | 1.0000      | 0.3018          |
| Three-objective optimization<br>( $\bar{P}_s, \eta_s,$ and $\bar{E}_p$ )           | LINMAP                     | 0.5462                 | 2.2788    | 0.9178                  | 0.3056   | 0.9995      | 0.5597      | 0.3455          |
|  | TOPSIS                     | 0.5475                 | 2.2032    | 0.9226                  | 0.3042   | 1.0000      | 0.5819      | 0.3306          |
|  | Shannon Entropy            | 0.5475                 | 2.2032    | 0.9226                  | 0.3042   | 1.0000      | 0.5819      | 0.3306          |
| Three-objective optimization<br>( $\bar{P}_s, \eta_s,$ and $\bar{P}_d$ )           | LINMAP                     | 0.5885                 | 1.5360    | 0.9670                  | 0.2576   | 0.8903      | 0.8775      | 0.1648          |
|  | TOPSIS                     | 0.5968                 | 1.4652    | 0.9658                  | 0.2462   | 0.8475      | 0.9161      | 0.1735          |
|  | Shannon Entropy            | 0.6611                 | 1.2679    | 0.9124                  | 0.1875   | 0.6095      | 1.0000      | 0.3022          |
| Three-objective optimization<br>( $\bar{P}_s, \bar{E}_p,$ and $\bar{P}_d$ )        | LINMAP                     | 0.6030                 | 1.5375    | 0.9835                  | 0.2512   | 0.8802      | 0.8889      | 0.1641          |
|  | TOPSIS                     | 0.6030                 | 1.5375    | 0.9835                  | 0.2512   | 0.8802      | 0.8889      | 0.1641          |
|  | Shannon Entropy            | 0.6610                 | 1.2686    | 0.9129                  | 0.1877   | 0.6106      | 1.0000      | 0.3016          |
| Three-objective optimization<br>( $\eta_s, \bar{E}_p,$ and $\bar{P}_d$ )           | LINMAP                     | 0.5718                 | 1.2686    | 0.9502                  | 0.2663   | 0.9017      | 0.8509      | 0.1756          |
|  | TOPSIS                     | 0.5852                 | 1.5303    | 0.9653                  | 0.2584   | 0.8890      | 0.8766      | 0.1663          |
|  | Shannon Entropy            | 0.6610                 | 1.2686    | 0.9129                  | 0.1877   | 0.6106      | 1.0000      | 0.3016          |
| Two-objective optimization<br>( $\bar{P}_s$ and $\eta_s$ )                         | LINMAP                     | 0.5407                 | 2.1898    | 0.9095                  | 0.3082   | 0.9988      | 0.5771      | 0.3367          |
|  | TOPSIS                     | 0.5531                 | 2.2047    | 0.9325                  | 0.3008   | 0.9992      | 0.5877      | 0.3250          |
|  | Shannon Entropy            | 0.4208                 | 3.6089    | 0.3745                  | 0.3718   | 0.4962      | 0.1442      | 0.8630          |
| Two-objective optimization<br>( $\bar{P}_s$ and $\bar{E}_p$ )                      | LINMAP                     | 0.5793                 | 1.9746    | 0.9740                  | 0.2820   | 0.9786      | 0.6855      | 0.2580          |
|  | TOPSIS                     | 0.5783                 | 1.9812    | 0.9728                  | 0.2827   | 0.9799      | 0.6824      | 0.2600          |
|  | Shannon Entropy            | 0.5476                 | 2.2031    | 0.9227                  | 0.3042   | 1.0000      | 0.5820      | 0.3305          |
| Two-objective optimization<br>( $\bar{P}_s$ and $\bar{P}_d$ )                      | LINMAP                     | 0.6459                 | 1.3747    | 0.9647                  | 0.2141   | 0.7360      | 0.9752      | 0.2286          |
|  | TOPSIS                     | 0.6468                 | 1.3629    | 0.9608                  | 0.2120   | 0.7257      | 0.9796      | 0.2345          |
|  | Shannon Entropy            | 0.6610                 | 1.2686    | 0.9129                  | 0.1877   | 0.6107      | 1.0000      | 0.3016          |
| Two-objective optimization<br>( $\eta_s$ and $\bar{E}_p$ )                         | LINMAP                     | 0.5026                 | 2.6195    | 0.7965                  | 0.3341   | 0.9482      | 0.4226      | 0.4700          |
|  | TOPSIS                     | 0.5079                 | 2.5508    | 0.8154                  | 0.3306   | 0.9605      | 0.4442      | 0.4491          |
|  | Shannon Entropy            | 0.5475                 | 2.2033    | 0.9226                  | 0.3042   | 1.0000      | 0.5819      | 0.3306          |
| Two-objective optimization<br>( $\eta_s$ and $\bar{P}_d$ )                         | LINMAP                     | 0.5709                 | 1.5216    | 0.9439                  | 0.2835   | 0.8861      | 0.8620      | 0.1782          |
|  | TOPSIS                     | 0.5898                 | 1.4515    | 0.9551                  | 0.2471   | 0.8410      | 0.9144      | 0.1792          |
|  | Shannon Entropy            | 0.6614                 | 1.2682    | 0.9126                  | 0.1875   | 0.6098      | 1.0000      | 0.3021          |
| Two-objective optimization<br>( $\bar{E}_p$ and $\bar{P}_d$ )                      | LINMAP                     | 0.5989                 | 1.5332    | 0.9797                  | 0.2527   | 0.8821      | 0.8879      | 0.1636          |
|  | TOPSIS                     | 0.5984                 | 1.5217    | 0.9777                  | 0.2518   | 0.8772      | 0.8928      | 0.1642          |
|  | Shannon Entropy            | 0.6610                 | 1.2686    | 0.9129                  | 0.1877   | 0.6106      | 1.0000      | 0.3016          |
| Maximum $\bar{P}_s$  | -                          | 0.6229                 | 1.7047    | 1.0000                  | 0.2501   | 0.8909      | 0.8152      | 0.1978          |
| Maximum $\eta_s$   | -                          | 0.4213                 | 3.6042    | 0.3777                  | 0.3718   | 0.5003      | 0.1456      | 0.8624          |
| Maximum $\bar{E}_p$  | -                          | 0.5469                 | 2.2063    | 0.9213                  | 0.3046   | 1.0000      | 0.5803      | 0.3319          |
| Maximum $\bar{P}_d$  | -                          | 0.6626                 | 1.2676    | 0.9121                  | 0.1870   | 0.6078      | 1.0000      | 0.3032          |
| Positive ideal point   | -                          | -                      | -         | 1.0000                  | 0.3718   | 1.0000      | 1.0000      | -               |
| Negative ideal point   | -                          | -                      | -         | 0.3745                  | 0.1854   | 0.4962      | 0.1442      | -               |



(a)

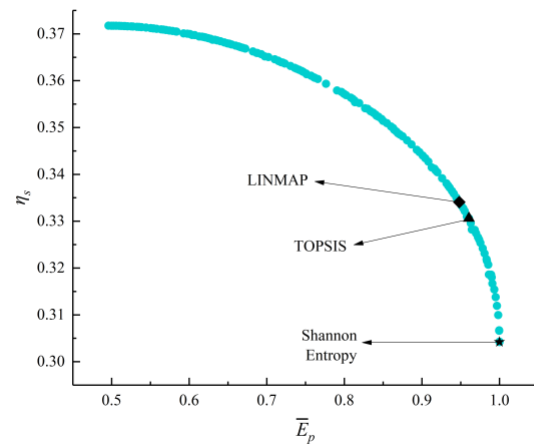


(b)

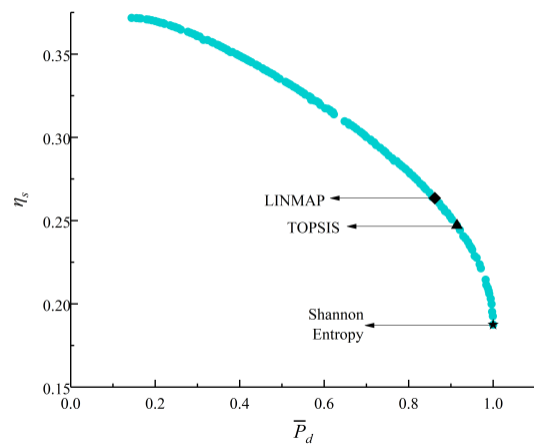


(c)

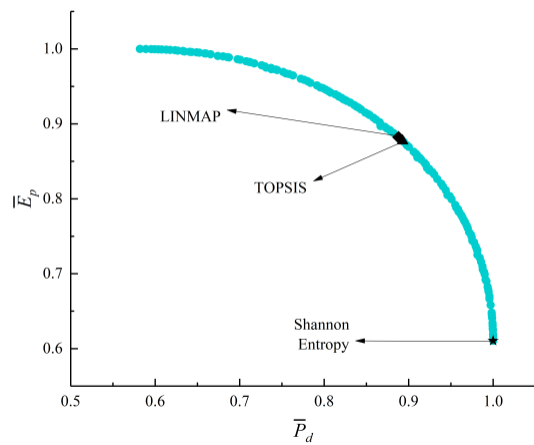
Figure 4. Cont.



(d)



(e)



(f)

**Figure 4.** Results for two-objective combinatorial optimizations. (a)  $\bar{P}_s - \eta_s$  Pareto frontier, (b)  $\bar{P}_s - \bar{E}_p$  Pareto frontier, (c)  $\bar{P}_s - \bar{P}_d$  Pareto frontier, (d)  $\eta_s - \bar{E}_p$  Pareto frontier, (e)  $\eta_s - \bar{P}_d$  Pareto frontier, and (f)  $\bar{E}_p - \bar{P}_d$  Pareto frontier.

Figure 5 shows the Pareto frontiers reached by corresponding three-objective optimizations ( $\bar{P}_s - \eta_s - \bar{E}_p$ ,  $\bar{P}_s - \eta_s - \bar{P}_d$ ,  $\bar{P}_s - \bar{E}_p - \bar{P}_d$ , and  $\eta_s - \bar{E}_p - \bar{P}_d$ ). As  $\bar{P}_s$  grows,  $\eta_s$  will decline,  $\bar{E}_p$  and  $\bar{P}_d$  will all first grow and then decline. As  $\eta_s$  grows,  $\bar{P}_d$  will decline,  $\bar{E}_p$  will

first grow and then decline. According to Table 2, when MOO is performed on  $\bar{P}_s - \eta_s - \bar{E}_p$ , the deviation indexes (0.3306) calculated by the TOPSIS and Shannon Entropy strategies are the same and smaller than that (0.3455) reached by the LINMAP strategy. When MOO is performed on  $\bar{P}_s - \eta_s - \bar{P}_d$ , the deviation index (0.1648) reached by the LINMAP strategy is smaller. When MOO is performed on  $\eta_s - \bar{E}_p - \bar{P}_d$ , the deviation index (0.1663) reached by the TOPSIS strategy is smaller. When MOO is performed on  $\bar{P}_s - \bar{E}_p - \bar{P}_d$ , the deviation indexes (0.1641) reached by the LINMAP and TOPSIS strategies are the same and smaller.

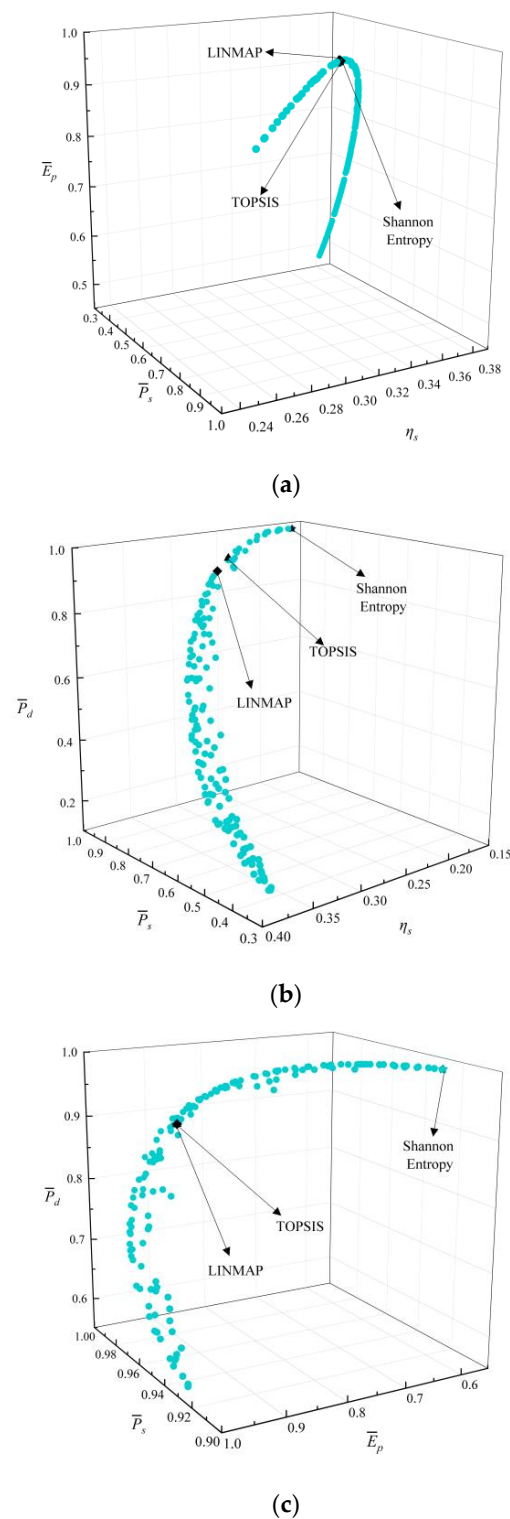
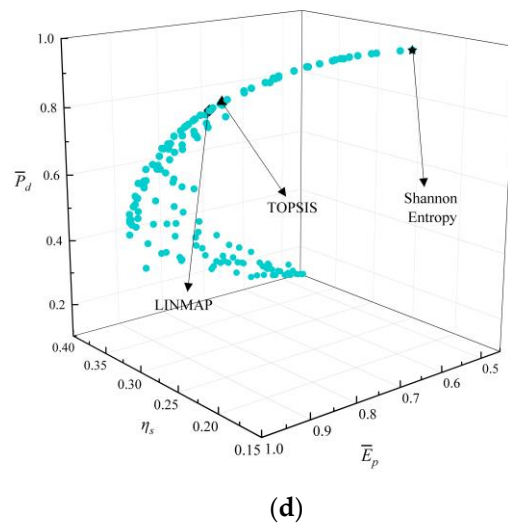
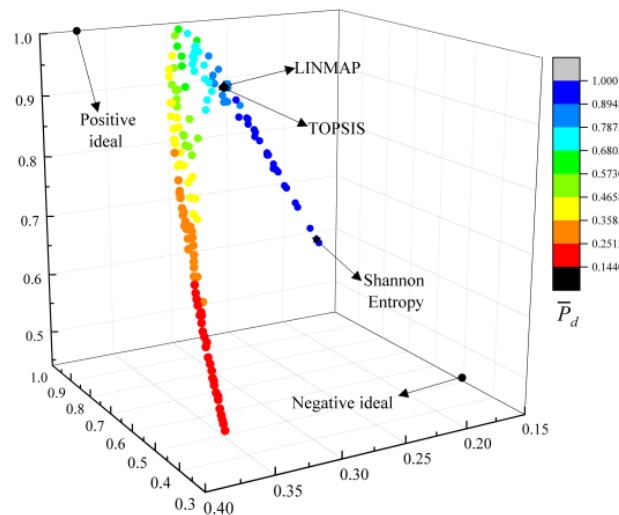


Figure 5. Cont.



**Figure 5.** Results for three-objective combinatorial optimizations. (a)  $\bar{P}_s - \eta_s - \bar{E}_p$  Pareto frontier, (b)  $\bar{P}_s - \eta_s - \bar{P}_d$  Pareto frontier, (c)  $\bar{P}_s - \bar{E}_p - \bar{P}_d$  Pareto frontier, and (d)  $\eta_s - \bar{E}_p - \bar{P}_d$  Pareto frontier.

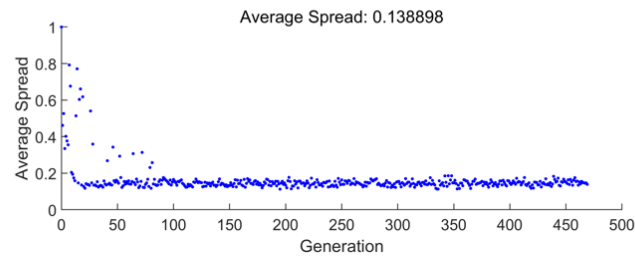
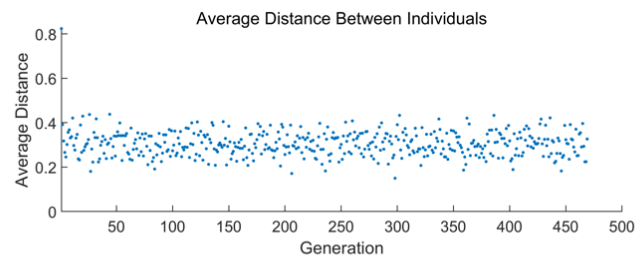
Figure 6 shows the Pareto frontier reached by four-objective optimization ( $\bar{P}_s - \eta_s - \bar{E}_p - \bar{P}_d$ ). From Figure 6, the three axes stand in for the values of the  $\bar{P}_s$ ,  $\eta_s$ , and  $\bar{E}_p$ , respectively, and the change of the value of  $\bar{P}_d$  is represented by the change in color on the Pareto frontier. The positive and negative ideal points are the points where the four OOs reach the best or worst values at the same time. It can be found that there are no optimal or worst  $x$  and  $\lambda$  to make the four OOs all reach the maximum or minimum at the same time. As  $\bar{P}_s$  grows,  $\eta_s$  will decline, and  $\bar{E}_p$  and  $\bar{P}_d$  will first grow and then decline.



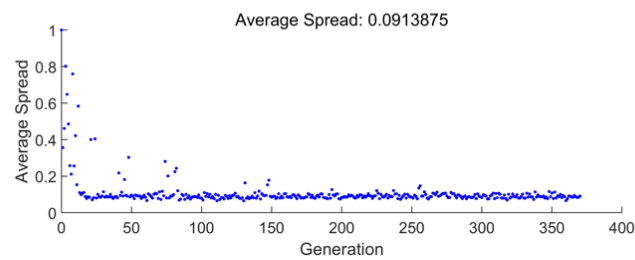
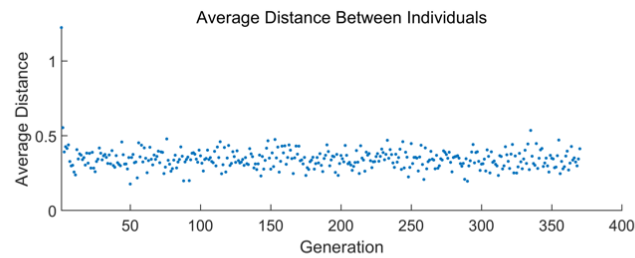
**Figure 6.**  $\bar{P}_s - \eta_s - \bar{E}_p - \bar{P}_d$  Pareto frontier.

Table 2 shows that when performing MOO on  $\bar{P}_s - \eta_s - \bar{E}_p - \bar{P}_d$ , the deviation indexes reached by TOPSIS and LINMAP strategies are smaller and their results are superior to those of the Shannon Entropy strategy.

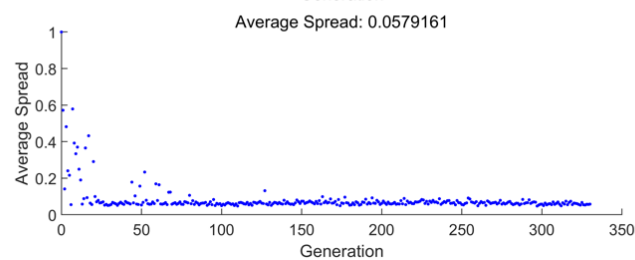
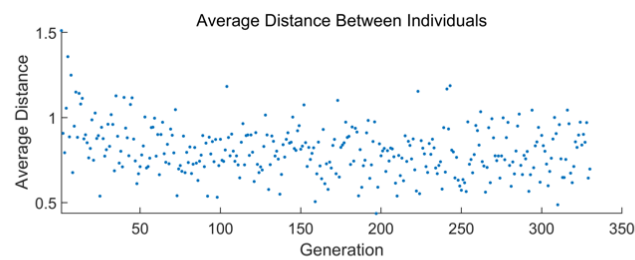
Figure 7 shows the average distance and spread versus the number of generations for three different MOOs ( $\bar{E}_p - \bar{P}_d$ ,  $\bar{P}_s - \bar{E}_p - \bar{P}_d$ , and  $\bar{P}_s - \eta_s - \bar{E}_p - \bar{P}_d$ ). From Figure 7a–c, when the genetic algorithm approaches convergence, which happens at 470th, 371st, and 331st generations for  $\bar{E}_p - \bar{P}_d$ ,  $\bar{P}_s - \bar{E}_p - \bar{P}_d$ , and  $\bar{P}_s - \eta_s - \bar{E}_p - \bar{P}_d$  optimizations, respectively, the genetic algorithm ends immediately.



(a)



(b)



(c)

**Figure 7.** Average distance and spread versus the number of generations. (a)  $\bar{E}_p - \bar{P}_d$ , (b)  $\bar{P}_s - \bar{E}_p - \bar{P}_d$ , and (c)  $\bar{P}_s - \eta_s - \bar{E}_p - \bar{P}_d$ .

#### 4. Conclusions

On the basis of the model established in references [67,68] and the NSGA-II algorithm, this study performs thermodynamic analysis and MOO on an irreversible SHE with linear phenomenological HTL. We treated  $x$  and  $\lambda$  as optimization variables, and utilized four performance indicators, namely,  $\bar{P}_s$ ,  $\eta_s$ ,  $\bar{E}_p$ , and  $\bar{P}_d$ , which were treated as OOs. We utilized TOPSIS, LINMAP, and Shannon Entropy strategies to reach deviation indexes of MOO on different combinations of OOs. The results showed that:

1. From the expressions derived of the four OOs under linear phenomenological HTL it was found that  $P_s$ ,  $\eta_s$ , and  $E_p$  were obviously different from those in reference [69], which indicates that the change of HTL also fundamentally changes the performance indicators of the heat engine;
2. The deviation indexes calculated by TOPSIS and LINMAP decision-making strategies are both 0.1683 when MOO is performed on  $\bar{P}_s - \eta_s - \bar{E}_p - \bar{P}_d$ , which are smaller and the optimization results are better than the results using the Shannon Entropy strategy. Compared with the deviation indexes (0.1978, 0.8624, 0.3319, and 0.3032) calculated by single-objective optimization at maximum  $\bar{P}_s$ ,  $\eta_s$ ,  $\bar{E}_p$ , and  $\bar{P}_d$  conditions, the deviation indexes of MOO are smaller and their results are better;
3. When the genetic algorithm approaches convergence, which happens at the 331st generation for  $\bar{P}_s - \eta_s - \bar{E}_p - \bar{P}_d$  optimization, the genetic algorithm ends immediately. The average distance and spread gradually decrease from the beginning to the 25th generation, after which they remain stable until the end of the calculation. The average distance is mainly between 0.5~1.5, and the average spread keeps to nearly zero after the 25th generation, which suggests that the optimization process is nearly stable;
4. When performing triple-objective optimizations, the MOO results of  $\bar{P}_s - \bar{E}_p - \bar{P}_d$  are better than the other combinations. The average distance mainly ranges from 0 to 0.5, and the average spread keeps to nearly zero after the 15th generation. When performing double-objective optimizations, the MOO results of  $\bar{E}_p - \bar{P}_d$  are better than the other combinations. The average distance mainly ranges from 0.2 to 0.4, and the average spread keeps to nearly zero after the 20th generation;
5. Compared with single-objective optimization, MOO can better take different OOs into account by choosing appropriate decision-making strategies. For the results of different objective combinations, appropriate schemes can be selected according to the actual design and operation to meet the requirements under different working conditions;
6. FTT and MOO are effective tools to guide performance improvement and optimization for SHE cycles. The consideration of different HTLs is also necessary.

**Author Contributions:** Conceptualization, L.C.; data curation, Y.G.; funding acquisition, L.C.; methodology, H.X., L.C., Y.G. and H.F.; software, H.X., Y.G. and H.F.; supervision, L.C.; validation, H.X. and H.F.; writing—original draft preparation, H.X. and L.C.; and writing—reviewing and editing, L.C. All authors have read and agreed to the published version of the manuscript.

**Funding:** This work is supported by the National Natural Science Foundation of China (Project Nos. 52171317 and 51779262).

**Institutional Review Board Statement:** Not applicable.

**Informed Consent Statement:** Not applicable.

**Data Availability Statement:** Not applicable.

**Acknowledgments:** The authors wish to thank the academic editor and the reviewers for their careful, unbiased, and constructive suggestions which led to this revised manuscript.

**Conflicts of Interest:** The authors declare no conflict of interest.

## Nomenclature

|                 |   |
|-----------------|---|
| $B$             | Buffer space                                      |
| $C_i$           | Heat-leakage coefficient, W/K                     |
| $C_v$           | Molar constant volume specific heat capacity, W/K |
| $e$             | Mechanism effectiveness                           |
| $F$             | Flywheel  |
| $M$             | Mechanical device                                 |
| $n$             | Mole number, mol                                  |
| $R$             | Regenerator                                       |
| $R_u$           | Universal gas constant, J/(mol · K)               |
| $T$             | Temperature, K                                    |
| $t$             | Time duration of the process, s                   |
| $V$             | Volume, m <sup>3</sup>                            |
| $W_c$           | Compression work, J                               |
| $W_e$           | Expansion work, J                                 |
| $W_+$           | Positive piston work, J                           |
| $W_-$           | Negative piston work, J                           |
| Greek symbol    |   |
| $\alpha, \beta$ | Heat-transfer coefficient, W/K                    |
| $\lambda$       | Volume–compression ratio                          |
| $\eta_R$        | Efficiency of the regenerator                     |
| $\tau$          | Cycle period, s                                   |
| $\sigma$        | Entropy-generation rate, W/K                      |
| Subscripts      |   |
| <i>opt</i>      | Optimal   |
| Superscripts    |   |
| –               | Dimensionless                                     |
| EP              | Efficient power                                   |
| FTT             | Finite time thermodynamics                        |
| HT              | Heat transfer                                     |
| HTL             | Heat-transfer law                                 |
| MOO             | Multi-objective optimization                      |
| OO              | Optimization objective                            |
| PD              | Power density                                     |
| SHE             | Stirling heat engine                              |
| WF              | Working fluid                                     |

## References

- Curzon, F.L.; Ahlborn, B. Efficiency of a Carnot engine at maximum power output. *Am. J. Phys.* **1975**, *43*, 22–24. [[CrossRef](#)]
- Andresen, B. *Finite-Time Thermodynamics*; University of Copenhagen: København, Denmark, 1983.
- Hoffmann, K.H.; Burzler, J.M.; Schubert, S. Endoreversible thermodynamics. *J. Non Equilib. Thermodyn.* **1997**, *22*, 311–355.
- Chen, L.G.; Wu, C.; Sun, F.R. Finite time thermodynamic optimization or entropy generation minimization of energy systems. *J. Non Equilib. Thermodyn.* **1999**, *24*, 327–359. [[CrossRef](#)]
- Zhang, Y.; Lin, B.H.; Chen, J.C. Performance characteristics of an irreversible thermally driven Brownian microscopic heat engine. *Eur. Phys. J. B* **2006**, *53*, 481–485. [[CrossRef](#)]
- Açikkalp, E.; Aras, H.; Hepbasli, A. Advanced exergoenvironmental assessment of a natural gas-fired electricity generating facility. *Energy Convers. Manag.* **2014**, *81*, 112–119. [[CrossRef](#)]
- Açikkalp, E. Methods used for evaluation actual power generating thermal cycles and comparing them. *Int. J. Electr. Power Energy Syst.* **2015**, *69*, 85–89. [[CrossRef](#)]
- Ahmadi, M.H.; Ahmadi, M.A.; Pourfayaz, F. Thermal models for analysis of performance of Stirling engine: A review. *Renew. Sustain. Energy Rev.* **2017**, *68*, 168–184. [[CrossRef](#)]
- Yasunaga, T.; Ikegami, Y. Application of finite time thermodynamics for evaluation method of heat engines. *Energy Proc.* **2017**, *129*, 995–1001. [[CrossRef](#)]
- Kaushik, S.C.; Tyagi, S.K.; Kumar, P. *Finite Time Thermodynamics of Power and Refrigeration Cycles*; Springer: New York, NY, USA, 2018.
- Fontaine, K.; Yasunaga, T.; Ikegami, Y. OTEC maximum net power output using Carnot cycle and application to simplify heat exchanger selection. *Entropy* **2019**, *21*, 1143. [[CrossRef](#)]

12. Feidt, M.; Costea, M. Progress in Carnot and Chambadal modeling of thermomechanical engine by considering entropy and heat transfer entropy. *Entropy* **2019**, *21*, 1232. [[CrossRef](#)]
13. Patel, V.K.; Savsani, V.J.; Tawhid, M.A. *Thermal System Optimization*; Springer: Cham, Switzerland, 2019.
14. Gonca, G.; Genc, I. Performance simulation of a double-reheat Rankine cycle mercury turbine system based on exergy. *Int. J. Exergy* **2019**, *30*, 392–403. [[CrossRef](#)]
15. Gonca, G.; Sahin, B. Performance analysis of a novel eco-friendly internal combustion engine cycle. *Int. J. Energy Res.* **2019**, *43*, 5897–5911. [[CrossRef](#)]
16. Gonca, G.; Hocaoglu, M.F. Performance Analysis and Simulation of a Diesel-Miller Cycle (DiMC) Engine. *Arab. J. Sci. Eng.* **2019**, *44*, 5811–5824. [[CrossRef](#)]
17. Gonca, G.; Genc, I. Thermoecology-based performance simulation of a Gas-Mercury-Steam power generation system (GMSPGS). *Energy Convers. Manag.* **2019**, *189*, 91–104. [[CrossRef](#)]
18. Feidt, M. Carnot cycle and heat engine: Fundamentals and applications. *Entropy* **2020**, *22*, 348. [[CrossRef](#)] [[PubMed](#)]
19. Masser, R.; Hoffmann, K.H. Endoreversible modeling of a hydraulic recuperation system. *Entropy* **2020**, *22*, 383. [[CrossRef](#)]
20. Kushner, A.; Lychagin, V.; Roop, M. Optimal thermodynamic processes for gases. *Entropy* **2020**, *22*, 448. [[CrossRef](#)]
21. Berry, R.S.; Salamon, P.; Andresen, B. How it all began. *Entropy* **2020**, *22*, 908. [[CrossRef](#)]
22. Feidt, M.; Costea, M. Effect of machine entropy production on the optimal performance of a refrigerator. *Entropy* **2020**, *22*, 913. [[CrossRef](#)]
23. Ding, Z.M.; Ge, Y.L.; Chen, L.G.; Feng, H.J.; Xia, S.J. Optimal performance regions of Feynman's ratchet engine with different optimization criteria. *J. Non Equilib. Thermodyn.* **2020**, *45*, 191–207. [[CrossRef](#)]
24. Paul, R.; Hoffmann, K.H. A class of reduced-order regenerator models. *Energies* **2021**, *14*, 7295. [[CrossRef](#)]
25. Gonca, G.; Hocaoglu, M.F. Exergy-based performance analysis and evaluation of a dual-diesel cycle engine. *Therm. Sci.* **2021**, *25*, 3675–3685. [[CrossRef](#)]
26. Qi, C.Z.; Ding, Z.M.; Chen, L.G.; Ge, Y.L.; Feng, H.J. Modelling of irreversible two-stage combined thermal Brownian refrigerators and their optimal performance. *J. Non Equilib. Thermodyn.* **2021**, *46*, 175–189. [[CrossRef](#)]
27. Andresen, B.; Salamon, P. Future perspectives of finite-time thermodynamics. *Entropy* **2022**, *24*, 690. [[CrossRef](#)]
28. Gonca, G.; Sahin, B.; Genc, I. Investigation of maximum performance characteristics of seven-process cycle engine. *Int. J. Exergy* **2022**, *37*, 302–312. [[CrossRef](#)]
29. Gonca, G.; Sahin, B. Performance investigation and evaluation of an engine operating on a modified dual cycle. *Int. J. Energy Res.* **2022**, *46*, 2454–2466. [[CrossRef](#)]
30. Paul, R.; Hoffmann, K.H. Optimizing the piston paths of Stirling cycle cryocoolers. *J. Non Equilib. Thermodyn.* **2022**, *47*, 195–203. [[CrossRef](#)]
31. Blank, D.A.; Davis, G.W.; Wu, C. Power optimization of an endoreversible Stirling cycle with regeneration. *Energy* **1994**, *19*, 125–133. [[CrossRef](#)]
32. Chen, J.C. The effect of regenerative losses on the efficiency of a Stirling heat engine at maximum power output. *Int. J. Ambient Energy* **1997**, *18*, 107–112. [[CrossRef](#)]
33. Chen, J.C.; Yan, Z.J.; Chen, L.X.; Andresen, B. Efficiency bound of a solar-driven Stirling heat engine system. *Int. J. Energy Res.* **1998**, *22*, 805–812. [[CrossRef](#)]
34. Wu, F.; Chen, L.G.; Wu, C. Sun, F.R. Optimum performance of irreversible Stirling engine with imperfect regeneration. *Energy Convers. Manag.* **1998**, *39*, 727–732. [[CrossRef](#)]
35. Tlili, I.; Timoumi, Y.; Nasrallah, S.B. Thermodynamic analysis of the Stirling heat engine with regenerative losses and internal irreversibilities. *Int. J. Engine Res.* **2008**, *9*, 45–56. [[CrossRef](#)]
36. Tlili, I. Finite time thermodynamic evaluation of endoreversible Stirling heat engine at maximum power conditions. *Renew. Sustain. Energy Rev.* **2012**, *16*, 2234–2241. [[CrossRef](#)]
37. Li, Y.Q.; He, Y.L.; Wang, W.W. Optimization of solar-powered Stirling heat engine with finite-time thermodynamics. *Renew. Energy* **2011**, *36*, 421–427.
38. Ahmadi, M.H.; Ahmadi, M.A.; Mehrpooya, M. Investigation of the effect of design parameters on power output and thermal efficiency of a Stirling engine by thermodynamic analysis. *Int. J. Low Carb. Technol.* **2016**, *11*, 141–156. [[CrossRef](#)]
39. Ahmed, F.; Huang, H.L.; Khan, A.M. Numerical modeling and optimization of beta-type Stirling engine. *Appl. Therm. Eng.* **2019**, *149*, 385–400. [[CrossRef](#)]
40. Ramachandran, S.; Kumar, N.; Timmaraju, M.V. Thermodynamic analysis of solar low-temperature differential Stirling engine considering imperfect regeneration and thermal losses. *J. Sol. Energy Eng.* **2020**, *142*, 051012. [[CrossRef](#)]
41. Ahadi, F.; Azadi, M.; Biglari, M.; Madani, S.N. Study of coating effects on the performance of Stirling engine by non-ideal adiabatic thermodynamics modeling. *Energy Rep.* **2021**, *7*, 3688–3702. [[CrossRef](#)]
42. de Moura, E.F.; Henriques, I.B.; Ribeiro, G.B. Thermodynamic-dynamic coupling of a Stirling engine for space exploration. *Therm. Sci. Eng. Prog.* **2022**, *32*, 101320. [[CrossRef](#)]
43. Purkait, C.; Biswas, A. Performance of Heisenberg-coupled spins as quantum Stirling heat machine near quantum critical point. *Phys. Lett. A* **2022**, *442*, 128180. [[CrossRef](#)]
44. Kitaya, K.; Isobe, M. Molecular dynamics study of a nano-scale  $\beta$ -type Stirling engine. *J. Phys. Conf. Ser.* **2022**, *2207*, 012006. [[CrossRef](#)]

45. Sahin, B.; Kodal, A.; Yavuz, H. Efficiency of a Joule-Brayton engine at maximum power density. *J. Phys. D Appl. Phys.* **1995**, *28*, 1309. [[CrossRef](#)]
46. Chen, L.G.; Zheng, J.L.; Sun, F.R.; Wu, C. Performance comparison of an endoreversible closed variable temperature heat reservoir Brayton cycle under maximum power density and maximum power conditions. *Energy Convers. Manag.* **2002**, *43*, 33–43. [[CrossRef](#)]
47. Ust, Y. A comparative performance analysis and optimization of irreversible Atkinson cycle under maximum power density and maximum power conditions. *Int. J. Thermophys.* **2009**, *30*, 1001–1013. [[CrossRef](#)]
48. Gonca, G. Performance analysis and optimization of irreversible Dual-Atkinson Cycle Engine (DACE) with heat transfer effects under maximum power and maximum power density conditions. *Appl. Math. Model.* **2016**, *40*, 6725–6736. [[CrossRef](#)]
49. Karakurt, A.S.; Bashan, V.; Ust, Y. Comparative maximum power density analysis of a supercritical CO<sub>2</sub> Brayton power cycle. *J. Therm. Eng.* **2020**, *6*, 50–57. [[CrossRef](#)]
50. Yan, Z.J.  $\eta$  and P of a Carnot engine at maximum  $\eta$ . *Chin. J. Nat.* **1984**, *7*, 475. (In Chinese)
51. Yilmaz, T. A new performance criterion for heat engines: Efficient power. *J. Energy Inst.* **2006**, *79*, 38–41. [[CrossRef](#)]
52. Kumar, R.; Kaushik, S.C.; Kumar, R. Efficient power of Brayton heat engine with friction. *Int. J. Eng. Res. Technol.* **2013**, *6*, 643–650.
53. Patodi, K.; Maheshwari, G. Performance analysis of an Atkinson cycle with variable specific-heats of the working fluid under maximum efficient power conditions. *Int. J. Low Carbon Technol.* **2013**, *8*, 289–294. [[CrossRef](#)]
54. Nilavarasi, K.; Ponnurugan, M. Optimized efficiency at maximum figure of merit and efficient power of power law dissipative Carnot like heat engines. *J. Stat. Mech. Theory Exp.* **2021**, *2021*, 043208. [[CrossRef](#)]
55. Tian, L.; Chen, L.G.; Ren, T.T.; Ge, Y.L.; Feng, H.J. Optimal distribution of heat exchanger area for maximum efficient power of thermoelectric generators. *Energy Rep.* **2022**, *8*, 10492–10500. [[CrossRef](#)]
56. Ahmadi, M.H.; Hosseinzade, H.; Sayyaadi, H.; Mohammadi, A.H.; Kimiaghali, F. Application of the multi-objective optimization method for designing a powered Stirling heat engine: Design with maximized power, thermal efficiency and minimized pressure loss. *Renew. Energy* **2013**, *60*, 313–322. [[CrossRef](#)]
57. Ahmadi, M.H.; Mohammadi, A.H.; Dehghani, S.; Barranco-Jiménez, M.A. Multi-objective thermodynamic-based optimization of output power of Solar Dish-Stirling engine by implementing an evolutionary algorithm. *Energy Convers. Manag.* **2013**, *75*, 438–445. [[CrossRef](#)]
58. Ahmadi, M.H.; Ahmadi, M.A.; Pourfayaz, F.; Hosseinzade, H.; Acikkalp, E.; Tlili, I.; Feidt, M. Designing a powered combined Otto and Stirling cycle power plant through multi-objective optimization approach. *Renew. Sustain. Energy Rev.* **2016**, *62*, 585–595. [[CrossRef](#)]
59. Luo, Z.Y.; Sultan, U.; Ni, M.J.; Peng, H.; Shi, B.W.; Xiao, G. Multi-objective optimization for GPU3 Stirling engine by combining multi-objective algorithms. *Renew. Energy* **2016**, *94*, 114–125. [[CrossRef](#)]
60. Punnathanam, V.; Kotecha, P. Effective multi-objective optimization of Stirling engine systems. *Appl. Therm. Eng.* **2016**, *108*, 261–276. [[CrossRef](#)]
61. Hooshang, M.; Toghyani, S.; Kasaeian, A.; Moghadam, R.A.; Ahmadi, M.H. Enhancing and multi-objective optimising of the performance of Stirling engine using third-order thermodynamic analysis. *Int. J. Ambient Energy* **2018**, *39*, 382–391. [[CrossRef](#)]
62. Dai, D.D.; Yuan, F.; Long, R.; Liu, Z.C.; Liu, W. Performance analysis and multi-objective optimization of a Stirling engine based on MOPSOCD. *Int. J. Therm. Sci.* **2018**, *124*, 399–406. [[CrossRef](#)]
63. Ye, W.L.; Yang, P.; Liu, Y.W. Multi-objective thermodynamic optimization of a free piston Stirling engine using response surface methodology. *Energy Convers. Manag.* **2018**, *176*, 147–163. [[CrossRef](#)]
64. Shah, P.; Saliya, B.; Raja, B.; Patel, V. A multiobjective thermodynamic optimization of a nanoscale Stirling engine operated with Maxwell-Boltzmann gas. *Heat Transfer—Asian Res.* **2019**, *48*, 1913–1932. [[CrossRef](#)]
65. Shakouri, O.; Ahmadi, M.H.; Gord, M.F. Thermodynamic assessment and performance optimization of solid oxide fuel cell-Stirling heat engine-reverse osmosis desalination. *Int. J. Low Carbon Technol.* **2021**, *16*, 417–428. [[CrossRef](#)]
66. Ahmed, F.; Zhu, S.M.; Yu, G.Y.; Luo, E.C. A potent numerical model coupled with multi-objective NSGA-II algorithm for the optimal design of Stirling engine. *Energy* **2022**, *247*, 123468. [[CrossRef](#)]
67. Senft, J.R. Theoretical limits on the performance of Stirling engines. *Int. J. Energy Res.* **1998**, *22*, 991–1000. [[CrossRef](#)]
68. Senft, J.R. *Mechanical Efficiency of Heat Engines*; Cambridge University Press: Cambridge, UK, 2007.
69. Xu, H.R.; Chen, L.G.; Ge, Y.L.; Feng, H.J. Multi-objective optimization of Stirling heat engine with various heat transfer and mechanical losses. *Energy* **2022**, *256*, 124699. [[CrossRef](#)]
70. Wu, C. Power optimization of a finite-time solar radiant heat engine. *Int. J. Ambient Energy* **1989**, *10*, 145–150. [[CrossRef](#)]
71. Wu, C. Optimal power from a radiating solar-powered thermionic engine. *Energy Convers. Manag.* **1992**, *33*, 279–282. [[CrossRef](#)]
72. Goktun, S.; Ozkaynak, S.; Yavuz, H. Design parameters of a radiative heat engine. *Energy* **1993**, *18*, 651–655. [[CrossRef](#)]
73. Angulo-Brown, F.; Paez-Hernandez, R. Endoreversible thermal cycle with a nonlinear heat transfer law. *J. Appl. Phys.* **1993**, *74*, 2216–2219. [[CrossRef](#)]
74. Huleihil, M.; Andresen, B. Convective heat transfer law for an endoreversible engine. *J. Appl. Phys.* **2006**, *100*, 014911. [[CrossRef](#)]
75. Chen, L.G.; Li, J.; Sun, F.R. Generalized irreversible heat-engine experiencing a complex heat-transfer law. *Appl. Energy* **2008**, *85*, 52–60. [[CrossRef](#)]
76. Li, J.; Chen, L.G. Optimal configuration of finite source heat engine cycle for maximum output work with complex heat transfer law. *J. Non Equilib. Thermodyn.* **2022**, *47*, 433–441. [[CrossRef](#)]

77. Chen, L.G.; Xia, S.J. Heat engine cycle configurations for maximum work output with generalized models of reservoir thermal capacity and heat resistance. *J. Non Equilib. Thermodyn.* **2022**, *47*, 329–338. [[CrossRef](#)]
78. Ding, Z.M.; Chen, L.G.; Sun, F.R. Performance optimization of a linear phenomenological law system Stirling engine. *J. Energy Inst.* **2015**, *88*, 36–42. [[CrossRef](#)]
79. Deb, K.; Pratap, A.; Agarwal, S.; Meyarivan, T. A fast and elitist multiobjective genetic algorithm: NSGA-II. *IEEE Trans. Evol. Comput.* **2002**, *6*, 182–197. [[CrossRef](#)]
80. Yusuf, A.; Bayhan, N.; Tiryaki, H.; Hamawandi, B.; Toprak, M.S.; Ballikaya, S. Multi-objective optimization of concentrated photovoltaic-thermoelectric hybrid system via non-dominated sorting genetic algorithm (NSGA II). *Energy Convers. Manag.* **2021**, *236*, 114065. [[CrossRef](#)]
81. Xiao, W.; Cheng, A.D.; Li, S.; Jiang, X.B.; Ruan, X.H.; He, G.H. A multi-objective optimization strategy of steam power system to achieve standard emission and optimal economic by NSGA-II. *Energy* **2021**, *232*, 120953. [[CrossRef](#)]
82. Soleimani, S.; Eckels, S. Multi-objective optimization of 3D micro-fins using NSGA-II. *Int. J. Heat Mass Transfer* **2022**, *197*, 123315. [[CrossRef](#)]
83. Arora, R.; Kaushik, S.C.; Kumar, R.; Arora, R. Soft computing based multi-objective optimization of Brayton cycle power plant with isothermal heat addition using evolutionary algorithm and decision making. *Appl. Soft Comput.* **2016**, *46*, 267–283. [[CrossRef](#)]
84. Hwang, C.L.; Yoon, K. *Multiple Attribute Decision Making-Methods and Applications a State of the Art Survey*; Springer: New York, NY, USA, 1981.
85. Etghani, M.M.; Shojaeefard, M.H.; Khalkhali, A.; Akbari, M. A hybrid method of modified NSGA-II and Topsis to optimize performance and emissions of a diesel engine using biodiesel. *Appl. Therm. Eng.* **2013**, *59*, 309–315. [[CrossRef](#)]
86. Kamali, H.; Mehrpooya, M.; Mousavi, S.H.; Ganjali, M.R. Thermally regenerative electrochemical refrigerators decision-making process and multi-objective optimization. *Energy Convers. Manag.* **2022**, *252*, 115060. [[CrossRef](#)]
87. Sayyaadi, H.; Mehrabipour, R. Efficiency enhancement of a gas turbine cycle using an optimized tubular recuperative heat exchanger. *Energy* **2012**, *38*, 362–375. [[CrossRef](#)]
88. Khanmohammadi, S.; Musharavati, F. Multi-generation energy system based on geothermal source to produce power, cooling, heating, and fresh water: Exergoeconomic analysis and optimum selection by LINMAP method. *Appl. Therm. Eng.* **2021**, *195*, 117127. [[CrossRef](#)]
89. Guisado, J.; Morales, F.J.; Guerra, J. Application of Shannon's entropy to classify emergent behaviors in a simulation of laser dynamics. *Math. Comput. Modell.* **2005**, *42*, 847–854. [[CrossRef](#)]
90. Zang, P.C.; Chen, L.G.; Ge, Y.L.; Shi, S.S.; Feng, H.J. Four-objective optimization for an irreversible Porous Medium cycle with linear variation in working fluid's specific heat. *Entropy* **2022**, *24*, 1074. [[CrossRef](#)]